Tandem reactions on phase separated MnO_2 and C to enhance formaldehyde conversion to hydrogen

Peipei Zhang, Hanlei Sun, Xiuyuan Lu*, Rena Oh, Xiang Zhang, Tuo Zheng, Jile Fu, Nuowei Zhang, Ouardia Akdim, Alberto Roldan*, Xiaoyang Huang*, Binghui Chen*

*Corresponding author:

Xiuyuan Lu, E-mail: xiuyuan_lu@hotmail.com;

Alberto Roldan, E-mail: roldanmartineza@cardiff.ac.uk;

Xiaoyang Huang, E-mail: HuangX17@cardiff.ac.uk;

Binghui Chen, E-mail: chenbh@xmu.edu.cn.

College of Chemistry and Chemical Engineering, Xiamen University, Xiamen 361005, P. R. China

Peipei Zhang, Hanlei Sun, Xiang Zhang, Tuo Zheng, Jile Fu, Nuowei Zhang, Xiaoyang Huang, Binghui Chen

Cardiff Catalysis Institute, School of Chemistry, Cardiff University, Park Place, Cardiff CF10 3AT, Wales, UK

Xiuyuan Lu, Alberto Roldanz, Ouardia, Akdim, Xiaoyang Huang

Department of Chemistry, Seoul National University, Seoul, 08826, Republic of Korea

Rena Oh

Abstract

Hydrogen (H_2) generation from formaldehyde conversion to water and formate shows a unique advantage regarding the bi-functional reaction route. MnO_2 was reported to be an active catalytic material for this process, especially after coating with carbon composite for improved active site distribution. Here, we show the conversion of formaldehyde in two tandem half-reactions: the oxidative dehydrogenation (ODH) of formaldehyde and hydrogen evolution reaction (HER). β-MnO_2 in a physical mixture with carbon (*i.e.*, XC-72R, graphene) enhances both formaldehyde conversion (from 13% to 19.5%) and hydrogen productivity (from 22.35 μmol mg^{-1} h^{-1} to 33.86 μmol mg^{-1} h^{-1}) by a synergistic effect of the phase separation catalyst in terms of electron redistribution and transport over the active sites. The catalyst examination supported by DFT calculation shows relatively low activation energy and band gap of β-MnO_2 + C with a density of states spanning the Fermi level. The discovery of this novel synergistic catalytic effect, a phase separation catalyst with cooperative enhancement, provides new insight into the area of tandem catalysis.

Introduction

In electrocatalysis, the investigation of hydrogen (H_2) production is an essential subject concerning H_2, a clean energy source with zero carbon emission from water electrolysis[1-5]. Numerous efforts have been dedicated to looking for non-noble catalysts with low overpotential for hydrogen evolution reaction (HER) for environmental and economic reasons[6-10]. However, at present, the proportion of H_2 produced *via* electrolysis (3.9%) compared to the production *via* thermal catalytic reactions using fossil fuel (*ca* 96%) is still minor[11]. For this reason, scientists are looking for a more rational way to produce H_2 under reaction conditions similarly mild to the electrocatalytic process. Photocatalysis, combined with electrocatalytic pathways for H_2 evolution from biomass reformation has triggered increasing attention. However, its

limited efficiency and yield remain a challenge[12-15]. More recently, the oxidative dehydrogenation (ODH) of formaldehyde for the formation of both H_2 and formate showed unique advantages concerning a bi-functional catalytic system even at room temperature[16-20]. On one side, formaldehyde as an environmental pollutant can be converted *via* an ODH route to formate, while on the other side, H_2 energy can be obtained *via* the evolution process of those dehydrogenated H^* from formaldehyde. M. Prechtl *et al.* used isotopically labelled experiments with mass spectroscopy analysis and discovered that both formaldehyde and water act as hydride donors for the production of H_2 molecule[21].

There have been several active catalysts reported in the formaldehyde reforming process. However, developing non-noble metal catalysts with comparable activity remains a scientific challenge[22-25]. In this work, we found that the transition metal oxide β-MnO_2 had unique properties and advantages for formaldehyde reforming in an alkaline medium as MnO_2 was reported with high performance in using OH^- hydroxyls[19,26-28]. However, MnO_2 is a semiconductor with limited conducting capability and a relatively small surface area to be a viable heterogeneous catalyst. For this reason, many investigations have been carried out to fabricate the MnO_2 or some other semi-conductive catalyst with carbon black/graphene and assemble the two composites into a hybrid material[29-32]. Yang *et al.* worked on a nanostructure incorporating graphene and MnO_2 as a catalyst with improved active surface area and bringing a high amount of surface OH^- for the formaldehyde oxidation, reducing the activation energy to 39.5 kJ mol^{-1} than the MnO_2 alone of 65.5 kJ mol^{-1} [33].

Here, our study shows that the ODH of formaldehyde and the HER process could be coupled into a tandem reaction system over β-MnO_2. Furthermore, the rates of both reactions improve significantly through a physical mixture of β-MnO_2 and C. It was found the two materials contacted remained as separated phases during and after the reaction, synergistically promoting the formaldehyde conversion (1182 mg_{HCHO} g_{cat}^{-1} h^{-1}) to almost double the reported binary catalyst (600 mg_{HCHO} g_{cat}^{-1} h^{-1})[34]. The tandem

reaction of H_2 evolution is also enhanced (Productivity$_{(MnO_2+C)}$: 33.86 μmol mg^{-1} h^{-1}; Productivity$_{(MnO_2)}$: 22.35 μmol mg^{-1} h^{-1}) due to the electron redistribution and transfer from the formaldehyde ODH to HER over the C and β-MnO_2 interface. In contrast, such tandem catalysis declines by adding an insulating material boron nitride (BN) (Productivity$_{(BN)}$: 13.23 μmol mg^{-1} h^{-1}). The proposed electron transfer route is highly correlated to the collision between the particles of β-MnO_2 and C. Within the one-pot system under a vigorous stirring of 1000 rpm, the reagent solution and catalysts behave like a slurry which facilitates intimate contact between each component in the reaction. The discovery focuses on phase-separated cooperative catalysts operating in an alkaline medium for tandem reactions between ODH and HER, emphasizing a novel and rational approach to designing the multi-component catalyst modules in the environment and energy-related areas.

Results

Different crystal structures of MnO_2 and corresponding characterisations

Manganese oxides can exist in several different crystal structures, such as α-MnO_2, β-MnO_2 and δ-MnO_2, which consist of [MnO_6] octahedra sharing corners and edges[35]. According to the different ways in which [MnO_6] octahedra are linked, the resulting MnO_2 structures can be divided into chain-like tunnel structures (α- and β-crystal) and layered structures (δ-crystal). These different types of crystal structures will show distinct catalytic performance[36]. In this work, α-MnO_2, β_1-MnO_2, β_2-MnO_2 and δ-MnO_2 catalysts were synthesized successfully by the hydrothermal method, corresponding to JCPDS 44-0141 (α-MnO_2), JCPDS 24-0735 (β-MnO_2) and JCPDS 80-1098 (δ-MnO_2), respectively (see Method section) (Fig. 1a). It should be noted that the β_2-MnO_2 was prepared from the crystalline transformation of γ-MnO_2 after calcination at 350 °C[37], whereas, no noticeable crystal transformation was observed among the other three catalysts. Compared with β_2-MnO_2, the sharp and strait peaks, *i.e.*, (110), (101) and (211) of β_1-MnO_2 (Fig. 1a) were due to its good crystallization and large grain size.

However, the peak intensities of the corresponding crystal planes in β_2-MnO_2 become lower and broader, indicating the relatively disordered structure property, which may attribute to the low temperature of 90 °C in the hydrothermal preparation process[38]. In addition, BET analyses of N_2 adsorption and desorption were carried out to evaluate the specific surface areas of β_1-MnO_2 and β_2-MnO_2 (Supplementary Fig. 1). As a result of the different crystal sizes, β_2-MnO_2 exhibited a specific surface area of 43.08 m^2 g^{-1}, which is much higher than that of β_1-MnO_2 (8.28 m^2 g^{-1}).

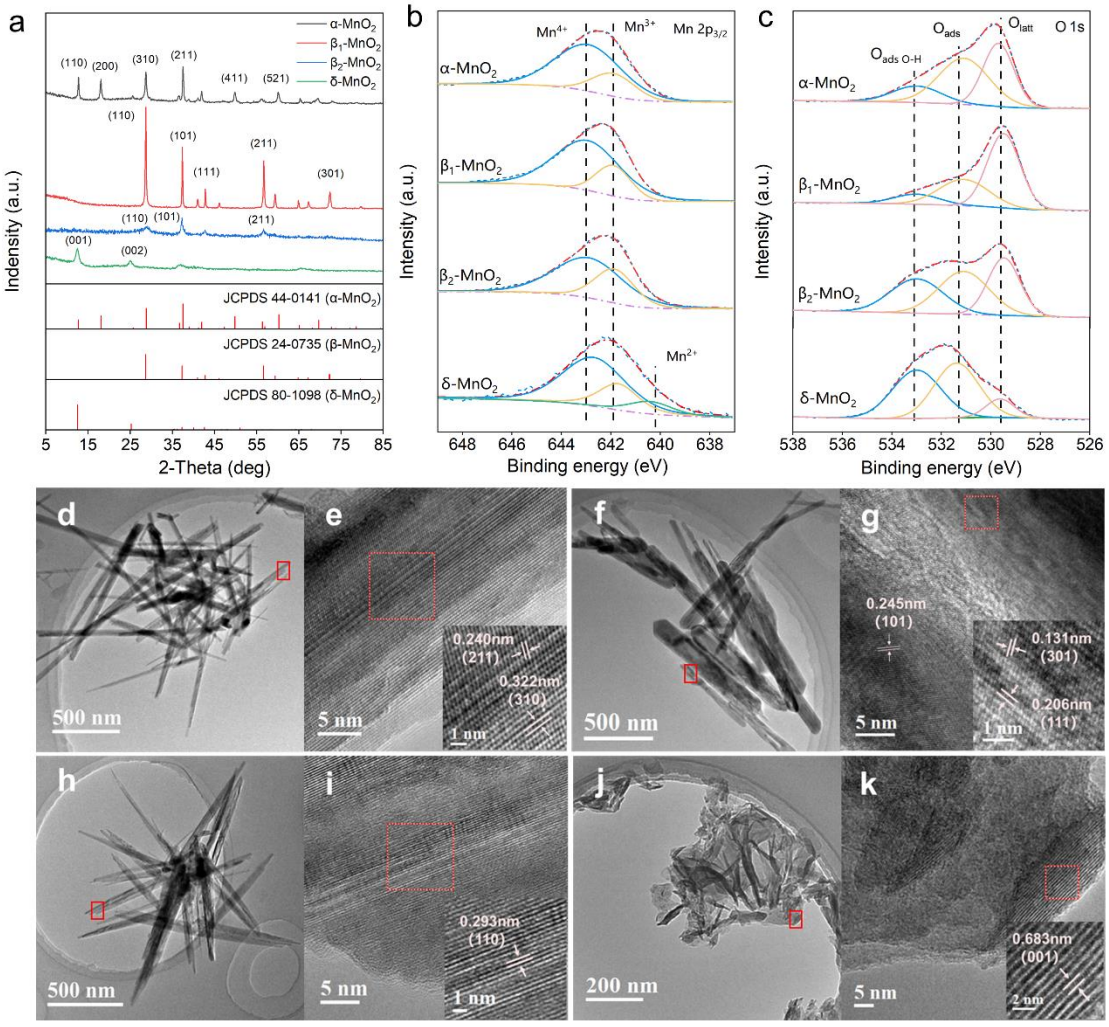

Fig. 1: Catalysts characterisation. a XRD patterns of α-MnO_2 (JCPDS 44-0141), β_1-MnO2 (JCPDS 24-0735), β_2-MnO2 (JCPDS 24-0735) and δ-MnO_2 (JCPDS 80-1098). XPS spectra of Mn $2p_{3/2}$ (**b**)and O 1s (**c**) for α-MnO_2, β_1-MnO_2, β_2-MnO_2 and δ-MnO_2.TEM images of α-MnO_2 (**d**), β_1-MnO_2 (**f**), β_2-MnO_2 (**h**) and δ-MnO_2 (**j**). HR-TEM images of α-MnO_2 (**e**), β_1-MnO_2 (**g**), β_2-MnO_2 (**i**) and δ-MnO_2 (**k**).

Transmission electron microscopy (TEM) images revealed that α-MnO_2, β_1-MnO_2 and β_2-MnO_2 were 1D chain-like nanowire structures, while δ-MnO_2 exhibited a layered appearance with the undulated and wrinkled surface (Figs. 1d, f, h and j). High-resolution transmission electron microscopy (HR-TEM) images showed the well-identified periodic lattice fringes of 0.240 nm and 0.322 nm are corresponding to the interplanar distance of (211) and (310) facets of α-MnO_2 (Fig. 1e). β_1-MnO_2 exhibited lattice fringes of 0.245 nm, 0.131 nm and 0.206 nm, which match well the interplanar distance of (101), (301) and (111) facets, respectively (Fig. 1g). Lattice fringes of 0.293 nm and 0.683 nm showed a typical (110) facet of β_2-MnO_2 and (001) facet of δ-MnO_2 (Figs. 1i and k). It was also worth noting that α-MnO_2, β_1-MnO_2 and β_2-MnO_2 grew along the crystal (310), (111) and (110) directions, respectively, while δ-MnO_2 grew layer-by-layer in all directions.

Apart from crystallinity and morphology, deconvoluted X-ray photoelectron spectroscopy (XPS) characterisation was carried out to investigate the surface chemical properties of the materials (Figs. 1b and 1c). The Mn 2p spectra demonstrated binding energies of around 642.3 eV corresponding to the Mn $2p_{3/2}$ species. The signals of Mn^{4+}, Mn^{3+} and Mn^{2+} cations can be observed after its deconvolution by using Gaussian fitting methods, where peaks are located at 642.9 eV, 641.9 eV and 640.2 eV respectively[39]. Among the detected chemical valences, the presence of Mn^{3+} cations is generally associated to the formation of oxygen vacancies due to the weaker Mn^{2+}-O and Mn^{3+}-O bonds than Mn^{4+}-O. The ratio of low valence Mn (Mn^{3+} and Mn^{2+}) follows the order: β_2-MnO_2 (0.326) > δ-MnO_2 (0.236) > β_1-MnO_2 (0.229) ≈ α-MnO_2 (0.229) (Supplementary Table 1). The relatively high amount of low Mn species generates a considerable quantity of longer and weaker Mn-O bonds on the β_2-MnO_2 surface. This indicates that surface oxygen atoms are more likely to be released to participate in oxidation reactions. In addition, the existence of low valence Mn^{3+} on the surface would also facilitate the activation of the surrounding oxygen atoms. The high-resolution XPS spectrum spanning the O 1s region for all the synthesized MnO_2 catalysts showed three major peaks at binding energies of 529.6 eV, 531.3 eV and 529.6 eV, corresponding to

the lattice oxygen (O_{latt}), surface adsorbed oxygen (O_{ads}) and surface hydroxyl oxygen ($O_{ads\ O\text{-}H}$) species[40], see Fig. 1c. The proportion of surface oxygen species (O_{ads} and $O_{ads\ O\text{-}H}$) for β_2-MnO_2 accounts 0.684, which is more than that of α-MnO_2 (0.624) and δ-MnO_2 (0.421). This result agrees well to the above analysis that Mn^{2+} and Mn^{3+} have a weak interaction to the surface O_{ads} and $O_{ads\ O\text{-}H}$. Besides, the high surface oxygen species proportion of δ-MnO_2 is probably due to its layered structure and large spacing between layers, which is formed by the intercalation of potassium ions with water molecules.

Catalytic performance of the MnO_2 catalysts

We tested the corresponding catalytic reactivity of the different MnO_2 crystals in alkaline formaldehyde (HCHO) solution at room temperature (experimental details in the Methods section). The HCHO conversion in a blank reaction (without MnO_2) was 3.98% (Fig. 2a), indicating a small number of auto-oxidation processes. The pH value of the post-reaction solution was 12.38, which is close to 12.42 of the fresh solution, meaning that few OH^- hydroxyls were consumed. The addition of MnO_2 materials into the reactor promoted the HCHO conversion in the following order: α-MnO_2 (C_{HCHO} = 11.74%), δ-MnO_2 (C_{HCHO} = 10.64%), β_1-MnO_2 (C_{HCHO} = 23.72%) and β_2-MnO_2 (C_{HCHO} = 25.32%). The pH value of the solutions with β-MnO_2 dropped to acidic conditions ($pH_{\beta_1\text{-}MnO_2}$ = 6.93, $pH_{\beta_2\text{-}MnO_2}$ = 6.48), while it was still alkaline in the presence of α-MnO_2 or δ-MnO_2 ($pH_{\alpha\text{-}MnO_2}$ = 11.64, $pH_{\delta\text{-}MnO_2}$ = 11.70). The difference in pH indicator that the formaldehyde should undergo a conversion process under the attack of OH^- hydroxyls. It was reported that the conversion of alkaline HCHO into formate accompanies the formation of H_2, this whole reaction can be illustrated as follow: $HCHO + OH^- \rightarrow HCOO^- + H_2$ [41,42]. Besides the reduction of pH, the β_2-MnO_2 catalyst exhibited definite hydrogen production (853.78 μmol after running a 6 h reaction) among the four MnO_2 catalysts (Fig. 2b). The H_2 production was 661.37 μmol for β_1-MnO_2, 164.00 μmol for α-MnO_2 and 95.14 μmol for δ-MnO_2.

To further study the hydrogen evolution activity of α-MnO_2 and β_2-MnO_2, linear sweep voltammetry (LSV) was performed under a similar condition to the thermal chemical reaction (in 0.1 M KOH, pH 13; see the Methods section) (Figs. 2c and 2d). The onset potential (overpotential for H_2 evolution) of α-MnO_2 and β_2-MnO_2 reached respectively -0.80 V and -0.70 V *vs* RHE, which confirmed a better performance of β_2-MnO_2 in HER as a half-reaction. Moreover, a smaller slope in the Tafel plots of β_2-MnO_2 (172.8 mV dec^{-1}) is obtained at a current density of 10 mA cm^{-2} than that of α-MnO_2 (295.1 mV dec^{-1}), indicating a higher rate of electron transfer and proton reduction over the surface of β_2-MnO_2. All these results are consistent with the thermal catalytic tests. Here, the HER is defined as the half-reaction in formaldehyde conversion, where the whole reaction involves the oxidative dehydrogenation (ODH) of formaldehyde and hydrogen evolution as two compositions.

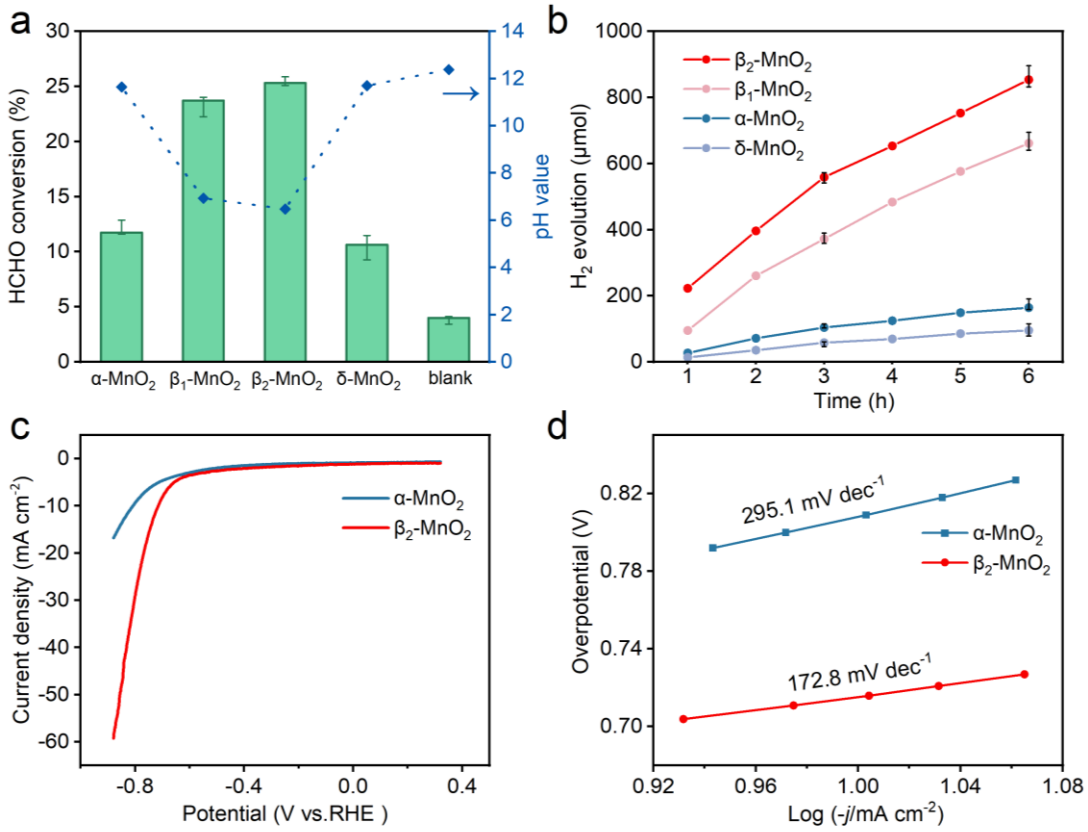

Fig. 2: Catalysts performance. a Formaldehyde conversion over α-MnO_2, β_1-MnO_2, β_2-MnO_2 and δ-MnO_2 samples with an amount of 50 mg, each reaction holds a pH value of 12.42 before reaction.

b Hydrogen evolution over α-MnO_2, β_1-MnO_2, β_2-MnO_2 and δ-MnO_2 samples as a catalyst with the amount of 10 mg. Associated error bars correspond to mean +/- SD (N = 3). **c** HER polarization curves of α-MnO_2 and β_2-MnO_2 (with IR compensation). **d** Tafel plots were obtained from the HER polarization curves. All reaction conditions regarding (**a-d**) were listed in the Method section.

Proposed tandem catalysis mechanism

Based on the oxidative dehydrogenation (ODH) of formaldehyde and hydrogen evolution reaction (HER) performance discussed above, we propose that the formaldehyde ODH and HER may follow a tandem pathway (Fig. 3) where a stable methanediol intermediate ($CH_2(OH)_2$) is formed *via* the formaldehyde hydration in water[43], subsequently, the whole reaction undergoes following steps:

1) $CH_2(OH)_2$ adsorbed on the MnO_2 surface deprotonates to form $H_2C(OH)O^*$ and H*;

2) The dissociated H* binds to a nearby metal on the same catalyst surface plane;

3) Promoted by OH^- in solution or on the surface, methanediol ($H_2C(OH)O^*$) proceeds another deprotonation to form the formate (HCOO*) and water, and another H* adsorbed on the Mn surface;

4) The methanediol reduction in step 3 provides the electrons to the nearby metals and H_2 is generated.

As such, the H_2 evolution reaction seems to be a tandem reaction following the formaldehyde ODH. Here, electron distribution over the catalyst surface plays an essential role in this process, which strongly links the two half-reactions. Therefore, materials with good electrical conductivity, such as XC-72R carbon black and graphene, should promote electron redistribution and transport and enhance the H_2 evolution.

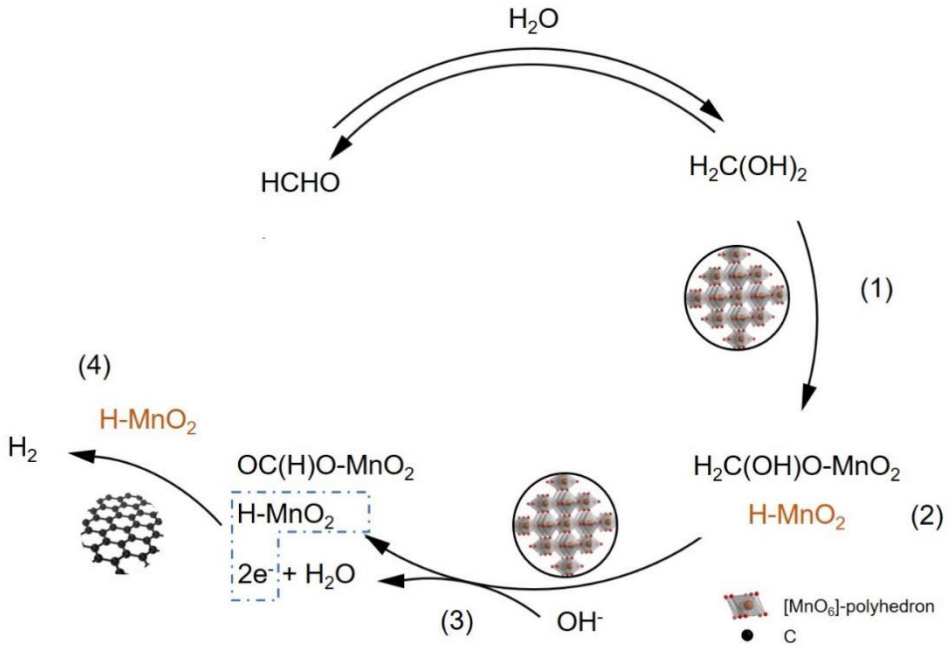

Fig. 3: Proposed mechanism investigation. Schematic representation of the H_2 evolution process in HCHO oxidation in the alkaline medium over a phase-separated catalyst of MnO_2 and C.

Enhanced tandem catalysis by physically mixing MnO_2 and carbon

Based on the aforementioned hypothesis, we combined β_2-MnO_2 with several materials of different conductivities, *i.e.*, conductors XC-72R carbon black and graphene, semiconductor TiO_2, and insulator BN. The powders of XC-72R carbon black and BN materials were compressed to thin wafers, and their electrical properties were measured by ST2742B Four-Point Probes. The conductivity of the XC-72R was 18.95 S cm^{-1} under 20 Mpa pressure, while that of BN was only 9.24×10^{-9} S cm^{-1}; obviously, XC-72R is a highly efficient conductor of electrons while BN is a poor conductor (Supplementary Figs. 2a and 2b).

Firstly, the corresponding H_2 evolution reaction was tested under the same reaction conditions using different materials mixed with β_2-MnO_2. The actual H_2 production was 792.3 μmol after a 75 min reaction when β_2-MnO_2 (25 mg) was used alone as the catalyst (Fig. 4a). Interestingly, using a physical mixture of β_2-MnO_2 and XC-72R (signed as β_2-MnO_2#XC), H_2 production was increased to 1057.8 μmol at 75 min (mixed

with 10 mg XC-72R). Little H_2 evolved over bare XC-72R (E_{75min}: 6.9 μmol) material in a blank reaction. The results showed that individual XC-72R has negligible catalytic activity, but it enhanced the catalytic performance of β_2-MnO_2. Similarly, the H_2 evolution on the graphene-β_2-MnO_2 mixture (signed as β_2-$MnO_2^{\#}$GE) was E_{75min}: 983.0 μmol, indicating an overall high efficiency, especially at the initial stage of the reaction (15 min-30 min). This may be because the layered larger area of graphene was beneficial to conducting electrons under vigorous stirring.

Compared to carbon materials, β_2-MnO_2 mixed with TiO_2 or BN exhibited relatively low H_2 production. There was little H_2 evolution generated over the pristine TiO_2 material (E_{75min}: 16.9 μmol) and BN material (E_{75min}: 2.8 μmol). The H_2 production was 699.0 μmol after a 75 min reaction on the mixture of β_2-MnO_2 and TiO_2 catalyst (signed as β_2-$MnO_2^{\#}TiO_2$), which had no significant difference from the value of bare β_2-MnO_2 catalyst. On the β_2-MnO_2 and BN mixture (signed as β_2-$MnO_2^{\#}$BN), no matter from the first sampling (E_{15min}: 66.7 μmol) or the fifth sampling (E_{75min}: 413.3 μmol), the H_2 evolution was always much lower than that for bare β_2-MnO_2 catalyst. Moreover, BN had suppressed the evolution of hydrogen significantly. Compared with a 60 min reaction (E_{60min}: 398.8.0 μmol), there was almost no increase in hydrogen production from 60 to 75 min (E_{75min}: 413.3 μmol).

Regarding the formaldehyde conversion on the mixture catalysts, we measured their activity and plotted the results in Fig. 4b. It can be seen that the catalytic trend follows the one for the HER: β_2-$MnO_2^{\#}$XC (C_{HCHO} = 19.48%) > β_2-MnO_2 (C_{HCHO} = 13.07%) > β_2-$MnO_2^{\#}$BN (C_{HCHO} = 7.61%), also in line with the change in pH of the post-reaction solution. All these results strongly indicated that the MnO_2 performance of the catalyst is enhanced through a simple method of mixing the β_2-MnO_2 and high conductive materials such as carbon, thanks to the improved electron transfer and distribution process. It positively affects the tandem processes between formaldehyde ODH and HER.

The XPS characterisation of a set of β_2-MnO_2 and β_2-$MnO_2^{\#}$XC catalyst samples (Fig. 4c) exhibits the Mn^{3+} proportion of 0.326, 0.455 and 0.332 in the fresh β_2-MnO_2, the

used β_2-MnO_2 and β_2-$MnO_2^{\#}$XC catalysts respectively (Supplementary Table 2). Typically, some Mn species would be reduced during the reaction, which means $Mn^{4+} \rightarrow Mn^{3+}$ due to the electron migration over the MnO_2 surface. However, the lower proportion of Mn^{3+} after reaction on the surface of β_2-$MnO_2^{\#}$XC compared to pristine β_2-MnO_2 suggests an improved distribution and transport of electrons over the additive XC-72R, thereby the Mn species were less reduced during the reaction. The XPS results support well the hypothesised reaction mechanism, which is further complemented by DFT calculations.

Besides, we have also compared our results with the most recent reported catalytic activities regarding the H_2 productivities. Indeed, the β_2-$MnO_2^{\#}$XC is the most reactive catalyst among all the non-noble catalysts, becoming competitive with those noble metal catalysts reported to date (Fig. 4d). Meanwhile, to show the advantage of the physical mixture structure in our study, another C-MnO_2 catalyst with hybrid nanostructure (signed as β_2-MnO_2/XC) was designed and prepared by in-situ growing the β-MnO_2 over the surface of C (see Methods section). However, its testing activity in H_2 production (3.6 μmol mg^{-1} h^{-1}) was observed to be about 10 folders lower compared to the physical mixing of β_2-$MnO_2^{\#}$XC (33.86 μmol mg^{-1} h^{-1}) (Fig. 4e). We think the poorer performance over the hybrid β_2-MnO_2/XC than their physical mixture is from the blocked Mn active sites by the incorporated carbon composite. For this reason, the catalyst morphology was characterized by HRTEM with elemental mapping, showing the success of incorporating β-MnO_2 on C grains (Figs. 5 a-g).

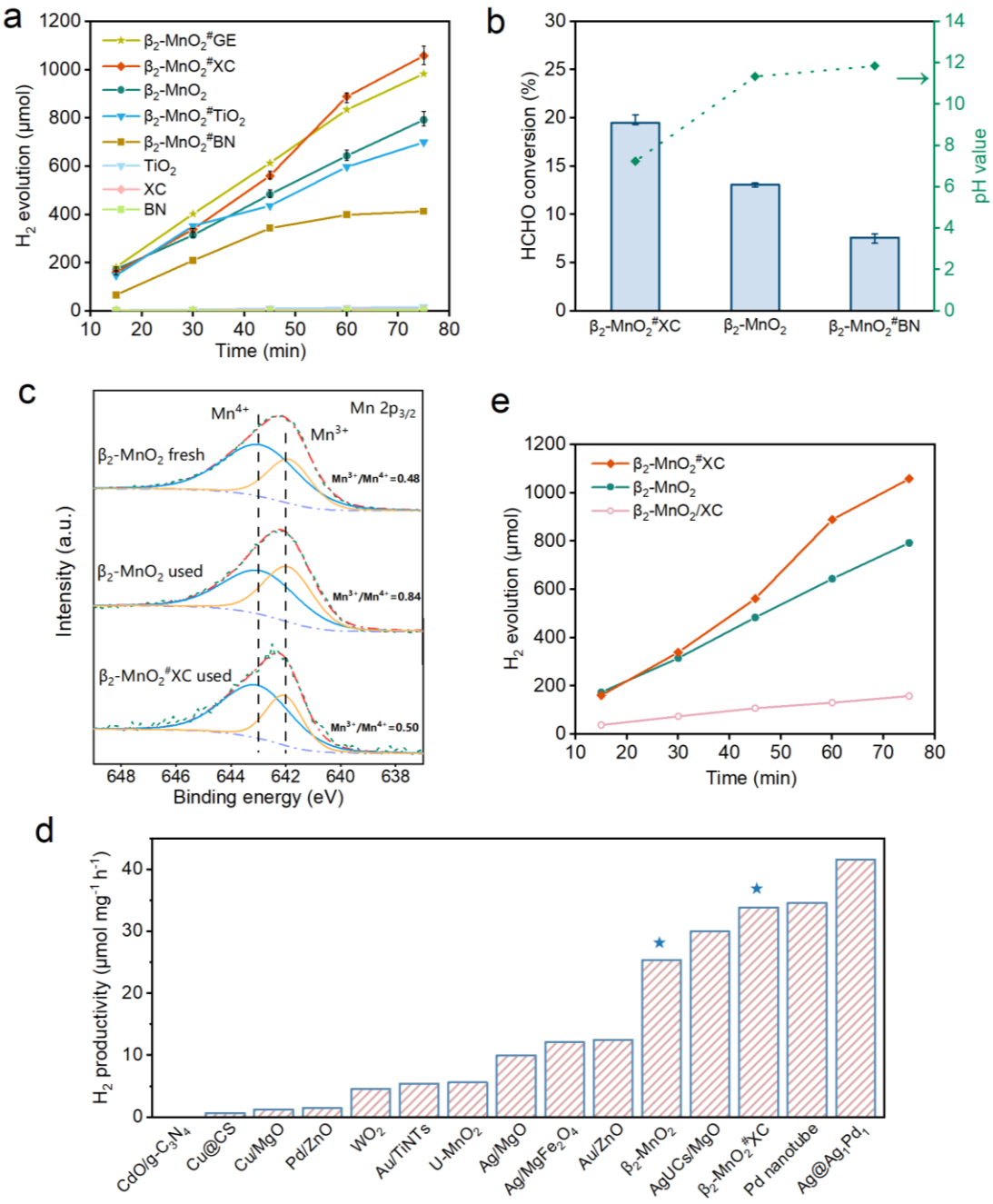

Fig. 4: Hydrogen evolution performance on the mixed catalysts. a Hydrogen evolution over 25 mg β_2-MnO_2 (β_2-MnO_2), 10 mg XC-72R carbon black (XC), 10 mg TiO_2 (TiO_2), physical mixture of 25 mg β_2-MnO_2 and 10 mg XC-72R (β_2-MnO_2#XC), physical mixture of 25 mg β_2-MnO_2 and 10mg graphene (β_2-MnO_2#GE), physical mixture of 25 mg β_2-MnO_2 and 25 mg BN (β_2-MnO_2#BN) samples. *Reaction conditions*: HCHO: 1 M, NaOH: 1 M, reaction temperature: 30 °C, stirring rate: 1000 rpm, O_2: 2 MPa. **b** Formaldehyde conversion on β_2-MnO_2, β_2-MnO_2#XC and β_2-MnO_2#BN samples as a catalyst with the amount of 50 mg MnO_2 and 25 mg XC or BN. The pH value of the solution was measured after the reaction. Associated error bars correspond to mean +/- SD (N = 3). **c** XPS spectra of the fresh β_2-MnO_2, the used β_2-MnO_2, and the used β_2-MnO_2#XC catalysts. **d**

Comparison of H_2 productivity upon HCHO oxidation with recent reports (CdO/g-C_3N_4[44], Cu@CS[45], Cu/MgO[46], Pd/ZnO[47], WO_2[48], Au/TiNTs[49], U-MnO_2[50], Ag/MgO[51], Ag/$MgFe_2O_4$[52], Au/ZnO[53], AgUCs/MgO[54], Pd nanotube[55], Ag@Ag_1Pd_1[55], β_2-MnO_2 and β_2-MnO_2#XC (bars marked with a star are for this work). **e** Hydrogen evolution over β_2-MnO_2/XC.

The post-reaction solution from β_2-MnO_2#XC presented a slurry form (Supplementary Fig. 3), which strengthens the importance of collision between the catalyst particles and the carbon co-catalyst in our study. Indeed, the positive synergistic effects from a physical mixture have been recently reported, *i.e.*, Au/Pd/C catalyst with a binary mixture structure showed higher catalysis than the corresponding Au-Pd alloy in hydroxymethylfurfural oxidation, which strongly correlates to the homogeneity among two phase-separated catalysts and their intimate contact through collision during reaction[56]. Here, to prove that the two catalysts were still phase-separated after the reaction, we collected the used β_2-MnO_2#XC catalyst and examined it with transmission electron microscopy (TEM) and Elemental mapping analysis (Fig. 5 and Supplementary Fig. 4). The long strip materials in the figures correspond to β_2-MnO_2 and the sheet-shaped materials assign to XC-72R (Figs.5 h-j). The corresponding EDX mapping showed heavy Mn, O and C signals in the mixture materials (Figs. 5 k-n), confirming that the two materials remain in a phase separation state after the reaction.

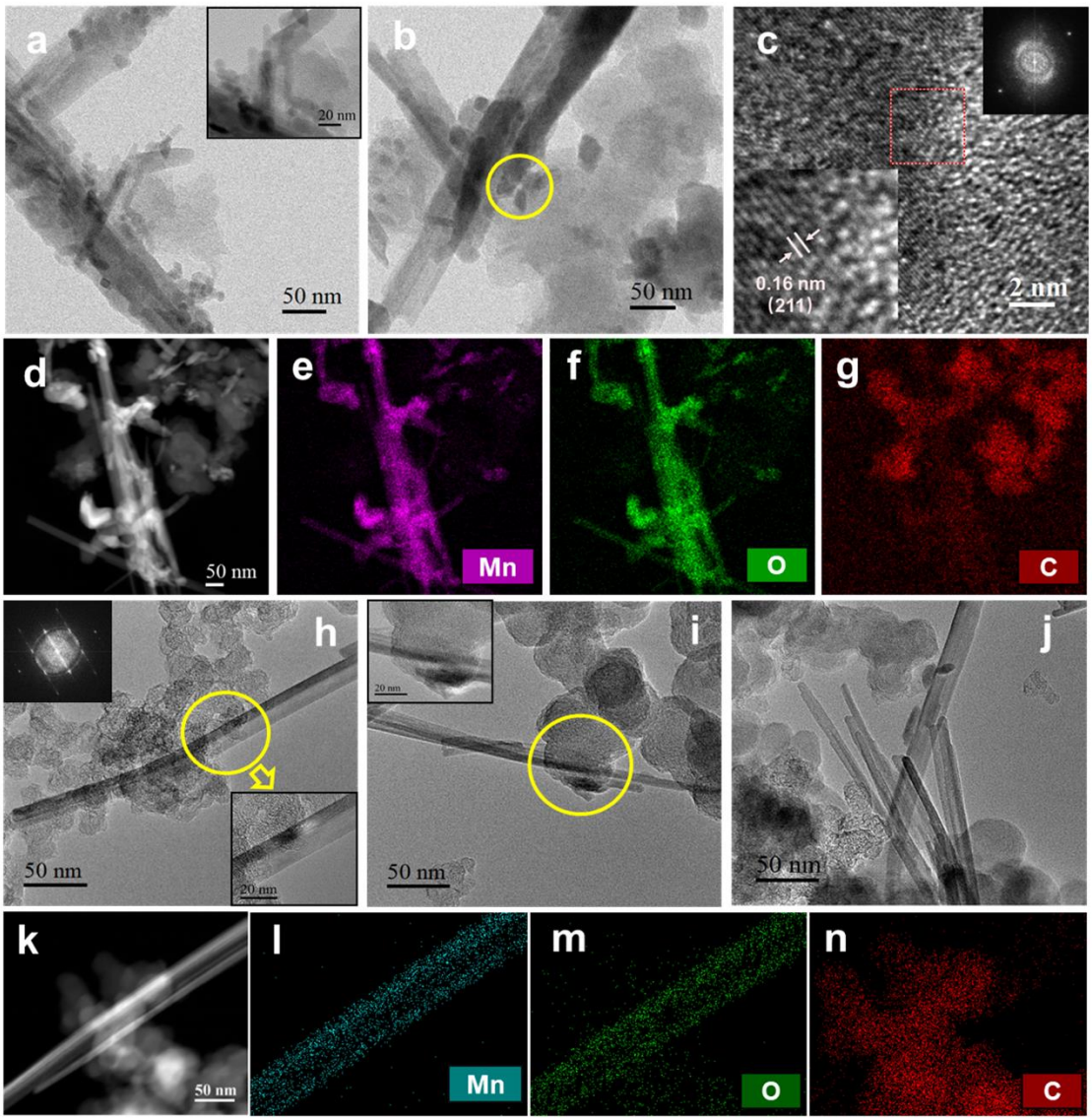

Fig. 5: Structural characterisations. a-c TEM and HRTEM images of β_2-MnO_2/XC catalyst with a hybrid structure. **d** HADDF-STEM image of β_2-MnO_2/XC catalyst. **e-g** Typical EDX mapping results of Mn, O, and C, respectively. **h-j** TEM images of used β_2-$MnO_2^{\#}$XC catalyst. **k** HADDF-STEM image of used β_2-$MnO_2^{\#}$XC catalyst. **l-n** Typical EDX mapping results of Mn, O, and C, respectively.

DFT calculation

Density functional theory (DFT) was used to model the geometric and electronic structure of catalytic materials used in the experiments. In particular, we focused on the crucial synergistic effect between MnO_2 and C on the tandem reactions of the formaldehyde ODH and the HER. We modelled the β_2-MnO_2 plane found in the XRD

patterns, i.e., (110) and (101) at the interface with a pristine graphene layer. Upon atomic relaxation, the electronic structure of the physical mixture and the effects on the reaction energy profile was investigated.

The density of states (DOS) shows the overlap between O 2p and Mn 3d corresponding to the Mn-O bond building the skeleton structure of β_2-MnO_2 (Fig. 6a and Supplementary Fig. 5). The DOS indicates the semiconductor properties of MnO_2 as the valence band and conductive band are separated by a gap of ~0.3 eV, in agreement with the previous report[57]. In contrast, the DOS of β_2-$MnO_{2\ (101)}$#C spans the Fermi level with a negligible band gap (Fig. 6b), demonstrating that the C addition as a physical mixture enhances the electron transfer on the β_2-MnO_2 surface. This argument also explains the results of a former study, where researchers found that the excellent conductivity of graphene helps the electrochemical adsorption of Li^+ ions on λ-MnO_2[58]. Besides the analysis of DOS, we have derived the charge difference analysis over the surface of β_2-$MnO_{2\ (101)}$#C. The representations in Fig. 5c suggest that the d_z^2 orbital of Mn atoms on the surface becomes activated due to the rearrangement of the MnO_2 electronic structure promoted by graphene. As a result, such d_z^2 orbital helps the electron movement (0.04 e.$Å^{-3}$ in terms of gaining and depleting of the electron) over the surface of the Mn atom. Meanwhile, the d_z^2 orbital also favours the adsorption of any intermediates during the formaldehyde ODH, *i.e.* the H* from dehydrogenations.

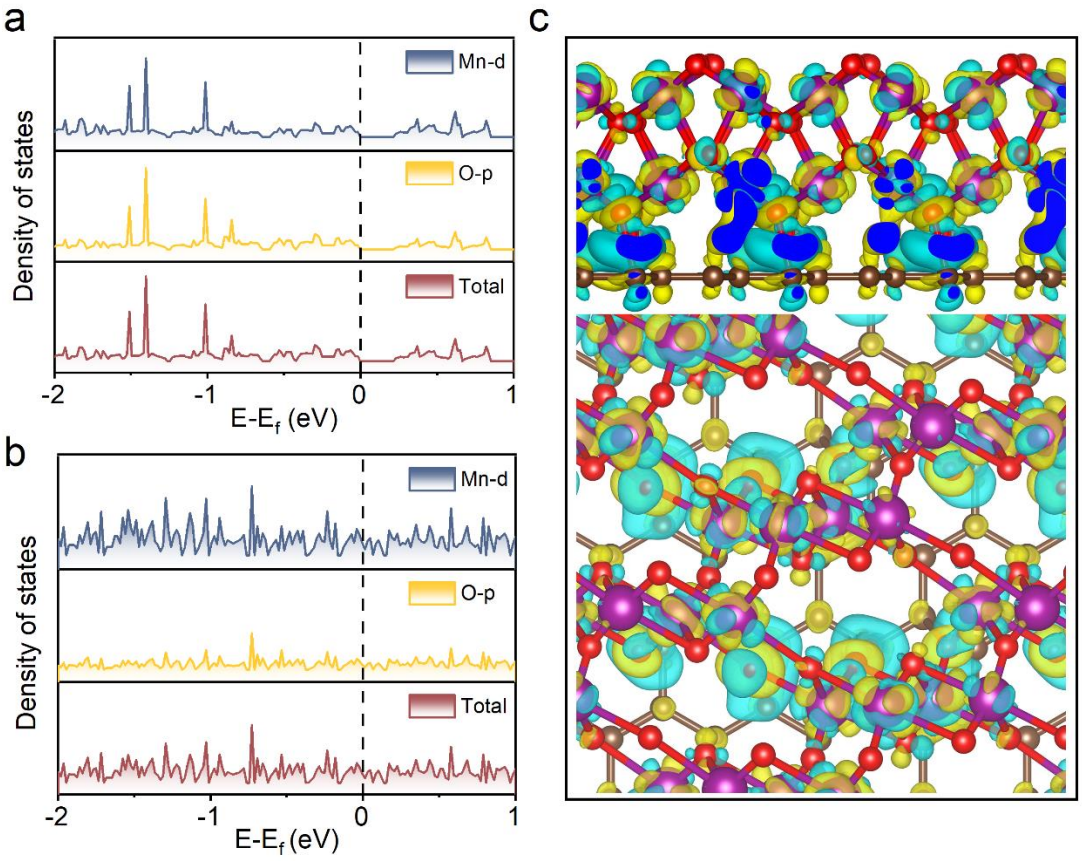

Fig. 6: β$_2$-MnO$_2$$^{\#}$C electronic structure. DOS and PDOS of β$_2$-MnO$_{2\ (101)}$ (**a**) and β$_2$-MnO$_2$$^{\#}$C (**b**). The dash lines refer to the Fermi level. **c** Side and top view of the partial charge density flow upon graphene adhesion. Yellow and green iso-surfaces (0.004 e.Å^{-3}) denote gain and depletion of electron density, respectively. Purple spheres represent Mn atoms, red spheres represent O atoms, khaki spheres represent C atoms.

The adsorption of H$_2$C(OH)O*, HCOO* and H* species on all non-equivalent adsorption sites were modelled and represented the most stable geometries (Supplementary Figs. 6 and 7). The overall energy profiles of formaldehyde conversion on β$_2$-MnO$_{2\ (101)}$ and β$_2$-MnO$_{2\ (101)}$$^{\#}$C surface were calculated and exhibited in Fig. 7. The reaction pathway of HCHO to HCOO* shows the generation of the intermediate H$_2$C(OH)O* is the rate-limiting step. On pristine β$_2$-MnO$_2$, this crucial step requires at least an energy input of 4.1 eV, whereas on β$_2$-MnO$_2$$^{\#}$C, it is just 2.2eV. The O-Mn bond upon H$_2$C(OH)O* adsorption on β$_2$-MnO$_{2\ (101)}$ is longer than on β$_2$-MnO$_{2\ (101)}$$^{\#}$C, 1.808 Å and 1.757 Å, respectively. The decrease in O-Mn bond length also indicates a strong

interaction between β_2-$MnO_{2\ (101)}$#C and the intermediates, which favours the pathway toward HCOO* formation.

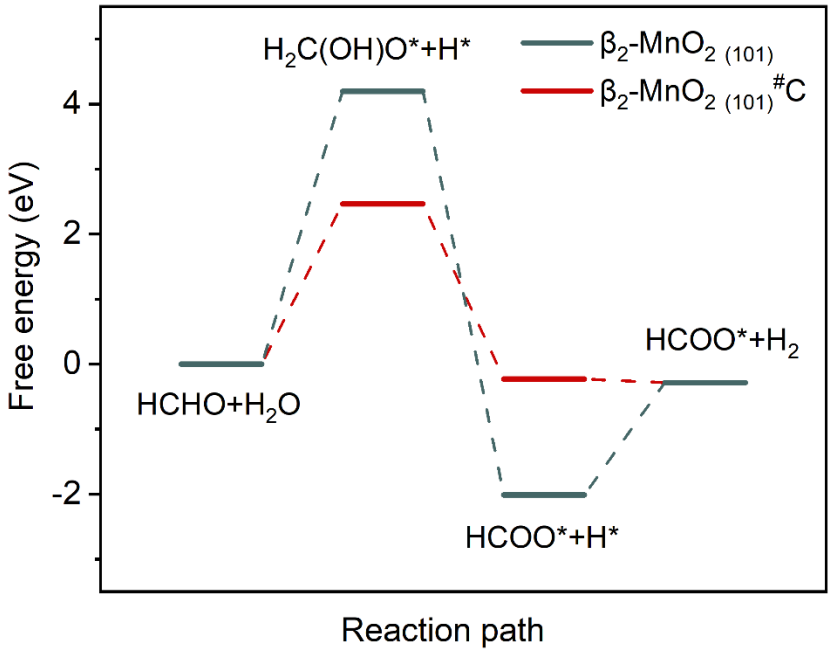

Fig. 7: ODH reaction energy profiles. Formaldehyde oxidation energy profile over the β_2-MnO_2 (blue line) and β_2-$MnO_{2\ (101)}$#C (red line).

Conclusions

In summary, we propose a concept of designing a multi-component with the phase-separated catalyst for tandem catalysis, which involves the composite of active MnO_2 catalyst and highly conductive carbon materials as co-catalyst sites for formaldehyde oxidative dehydrogenation (ODH) and hydrogen evolution reaction (HER). This prototype utilises the interaction between MnO_2 and carbon as a physical mixture, promoting the transfer and distribution of electrons from ODH to HER on the catalyst surface, and enhancing hydrogen production and the overall catalytic performance. β_2-MnO_2#XC as catalyst showed the highest hydrogen evolution productivity (33.86 μmol mg^{-1} h^{-1}) among the literature so far of non-noble catalysts. DFT calculation supports the experimental results and proves that the addition of carbon reduces the bandgap of

the composite system to 0 eV and decreases the reaction energy of the rate-limiting step of the reaction. This study directly demonstrates the effectiveness of using phase separation catalysts to improve active site distribution for linking two consecutive reactions, which could be relevant in many other areas of tandem catalysis where the physical mixture is yet to be deeply explored.

Methods

Chemicals (purity and source)

All chemicals were purchased from commercial suppliers and used as provided: $MnSO_4·H_2O$ (Energy Chemical, 99%), $(NH_4)_2S_2O_8$ (Macklin, >99%), $KMnO_4$ (Sinopharm, ≥99%), TiO_2 (Aladdin, ≥99%), BN (Aladdin, 99.9%), XC-72R carbon black (Cabot conductive carbon), graphene (Knano Graphene Technology, KNG-G2), formaldehyde aqueous solution (Sinopharm, with 8-14% methanol liquid), acetic acid (Sinopharm, >99.5%), ammonium acetate (Sinopharm, 98%) and acetylacetone (Sinopharm, 99%).

Preparation of the MnO_2 catalysts

All the MnO_2 catalysts were prepared by the hydrothermal method.

For α-MnO_2, 1.25 g $KMnO_4$ and 0.53 g $MnSO_4·H_2O$ were dissolved in the 80mL deionised water with magnetic stirring for about 40 min to form a homogeneous suspension. Then the resulting solution was instantly transferred into a 100 mL Teflon-lined stainless steel autoclave and maintained the temperature at 160 °C for 12 h. After cooling naturally, the resulting brown precipitate was collected by filtration and washed with deionised water several times. The product was dried at 80 °C for 8 h and then calcined at 350 °C in a muffle furnace for 2 h. The preparations of β1-MnO_2, β2-MnO_2, and δ-MnO_2 were similar to β-MnO_2, except for the reactants, reaction temperature, and reaction duration, see below.

β_1-MnO_2: 1.69 g $MnSO_4·H_2O$ and 2.28 g $(NH_4)_2S_2O_8$ were dissolved into the deionised water, and the reaction temperature was maintained at 140 °C for 12 h.

β_2-MnO_2: 3.38 g $MnSO_4·H_2O$ and 4.58 g $(NH_4)_2S_2O_8$ were dissolved into the deionised water, and the reaction temperature was maintained at 90 °C for 24 h.

δ-MnO_2: 1.50 g $KMnO_4$ and 0.28 g $MnSO_4·H_2O$ were dissolved into the deionised water, and the reaction temperature was maintained at 160 °C for 12 h.

Preparation of the β_2-MnO_2/XC catalyst

The catalyst was prepared by the hydrothermal method. 0.696 g XC-72R carbon black was added to the 80mL deionised water and sonicated for 2h. Then 3.38 g $MnSO_4 \cdot H_2O$ and 4.58 g $(NH_4)_2S_2O_8$ were added with magnetic stirring for about 40 min. The resulting solution was instantly transferred into a 100 mL Teflon-lined stainless steel autoclave and maintained the temperature at 90 °C for 24 h. After cooling naturally, the resulting precipitate was collected by filtration and washed with deionised water several times. The product was dried at 80 °C for 8 h and then calcined at 350 °C in a muffle furnace for 2 h.

H_2 evolution experiments

H_2 evolution reactions from alkaline HCHO solution were carried out in a stainless steel reactor (40 mL) equipped with a Teflon liner 2 mm thick and a self-contained magnetic stirrer. In a typical experiment, we add a certain amount of catalysts with 10 mL alkaline HCHO solution (1M) in the reactor. The O_2 pressure in the reactor was adjusted to be 2 MPa, and the reaction was maintained at room temperature (30 °C). The stirring rate of the magnetic spin bar was controlled at 1000 rpm. Then, gas evolution from the reactor (H_2 and O_2) was analyzed on a GC-9160 gas chromatography *via* a six-port valve gas sampler at regular time intervals (Supplementary Fig. 8). Nitrogen gas was used as carrier gas. To calculate the amount of H_2 evolution, we tested different concentrations of standard hydrogen gas and fitted a standard curve (Supplementary Fig. 9a).

HCHO conversion tests

The content of formaldehyde was determined by the acetylacetone spectrophotometric method. Preparation of Acetylacetone solution: 25 g ammonium acetate, 3 mL acetic acid, and 0.25 mL acetylacetone were added in a 100 ml volumetric flask, then dissolved with 100 mL deionised water.

In a typical test, we dilute the sample solution by a factor of 20. Then, 50 μL sample solution after dilution was accurately added in a 25 mL colourimetric tube, the volume was fixed to scale with deionised water and 2.5 mL acetylacetone solution was added. The colourimetric tube was then placed in a 58 °C water bath for 20 min and cooled down naturally for absorbance measurement at 414 nm on a UV-1750 UV-vis spectrophotometer. We also tested different concentrations of formaldehyde solution and fitted a standard curve (Supplementary Fig. 9b).

Electrode preparation

The glassy carbon electrode (GCE, 3 mm) was used as the working electrode. Carbon rod and saturated calomel electrode (SCE) were used as counter and reference electrodes. 4 mg of each catalyst mixed with 2 mg XC-72R carbon black, 900 μL of deionised H_2O and 100 μL of Nafion solution (5 wt.%) was prepared as an ink solution, followed by sonication for 10 min. Afterwards, 5 μL of ink solution was dropped onto the surface of GCE and dried under the atmosphere overnight to form an electrode.

Electrochemical tests

All electrochemical measurements were performed using a three-electrode system connected to a CHI 760E electrochemical workstation (Shanghai CHI Instruments Company) at 25 ℃. The graphite carbon rod and saturated calomel electrode (SCE) served as the counter electrode and reference electrode, respectively. Corresponding linear sweep voltammetry (LSV) curves were recorded at a scan rate of 20 mV s^{-1} from -0.7 V to -1.9 V (*vs* SCE) in 30 mL of 0.1M KOH (pH 13) after the polarization curves reached a steady state. All the measured potential values were converted to the reversible hydrogen electrode (RHE). The current density was normalized to the geometric electrode area (~ 0.07065 cm^2). All linear sweep voltammetry curves were recorded by IR compensation.

Catalyst structure characterisation

The crystal structure of the catalysts was analysed by X-ray diffraction (XRD) on a Rigaku X-ray diffractometer, using Cu Kα radiation source (35 kV and 20 mA) in a 2θ angular range of 5-85°. Transmission electron microscopy (TEM), high angle annular dark field-scanning transmission electron microscopy (HAADF-STEM) images and energy dispersive spectroscopy (EDS) maps were collected on a Talso transmission electron microscope working at an accelerating voltage of 200 kV. X-ray photoelectron spectroscopy (XPS) analysis was conducted using a Quantum 2000 scanning ESCA microprobe, which was equipped with a focused monochromatic Al Kα X-ray (1486.7 eV) source for excitation, a spherical section analyzer, and a 16-element multichannel detection system. The distributions of different Mn and O species are calculated based on the area of the peaks obtained from the deconvolution of the corresponding XPS spectra and the corresponding correction factor. The nitrogen adsorption and desorption experiments were performed on the Micromeritics ASAP 2020 instrument, and the Brunauer-Emmett-Teller (BET) equation was used to calculate the specific surface area. The electrical resistance of the XC-72R carbon and BN materials was measured by ST2742B Four-Point Probes and ST2643 high insulation resistance measuring

instrument (Suzhou, China) under a standard atmosphere. Each sample was measured three times and the mean was plotted.

DFT calculations

The Vienna Ab-initio Simulation Package (VASP) was employed to simulate the formaldehyde oxidation on β_2-MnO_2 and β_2-MnO_2#C within the DFT frameworks[59,60]. The spin-polarized revised Perdew-Burke-Ernzerhof (rPBE) method of the generalized gradient approximation (GGA) was adopted to describe the exchange-correlation with a plane-wave kinetic cutoff energy of 500 eV[61]. The projector augmented wave (PAW) includes non-spherical contributions from the core to the gradient corrections[62,63]. The long-range interactions were characterized by the DFT-D3 method of Grimme with zero dampings[64]. The convergence thresholds of internal forces and electronic relaxation were set to 0.02 eV.$Å^{-1}$ and 10^{-5} eV, respectively. A 3×3×1 k-spacing Monkhorst-Pack grid sampled the Brillouin zone with a smearing broadening of 0.2 eV. The optimized lattice parameter of pristine graphene and MnO_2 is 2.469 Å and 2.890 Å, respectively. All surfaces were represented by a supercell slab model, and we added 15 Å of vacuum perpendicular to the slab to prevent any spurious interaction with periodic images. Dipole correction perpendicular to the surface was applied upon the molecular adsorption. The DFT calculation tends to underestimate the band gap of systems containing d orbitals. We use the DFT + U spin polarization approach to address this problem with the U value of Mn set to 4.0 eV[65,66].

Data availability

All data presented in this study are included either in the article or in the Supplementary Information. The raw data are available from the corresponding authors upon request.

References

1. Yang, S. *et al.* Recent advances in electrocatalysis with phthalocyanines. *Chem. Soc. Rev.* (2021).
2. Chia, X. & Pumera, M. Characteristics and performance of two-dimensional materials for electrocatalysis. *Nature Catalysis*. **1**, 909-921 (2018).
3. Dai, J. *et al.* Hydrogen spillover in complex oxide multifunctional sites improves acidic hydrogen evolution electrocatalysis. *Nat. Commun.* **13**, 1-10 (2022).
4. Xu, Y. *et al.* Recent advances in electrocatalysts for neutral and large-current-density water electrolysis. *Nano Energy*. **80**, 105545 (2021).

5. Wei, C. *et al.* Recommended practices and benchmark activity for hydrogen and oxygen electrocatalysis in water splitting and fuel cells. *Adv. Mater.* **31**, 1806296 (2019).
6. Xiao, C. *et al.* High-index-facet-and high-surface-energy nanocrystals of metals and metal oxides as highly efficient catalysts. *Joule*. **4**, 2562-2598 (2020).
7. Yao, Q. *et al.* Channel-rich RuCu nanosheets for pH-universal overall water splitting electrocatalysis. *Angew. Chem.* **131**, 14121-14126 (2019).
8. Puente Santiago, A. R. *et al.* A new class of molecular electrocatalysts for hydrogen evolution: Catalytic activity of $M_3N@C_{2n}$ (2n = 68, 78, and 80) fullerenes. *J. Am. Chem. Soc.* **143**, 6037-6042 (2021).
9. Lee, W. H. *et al.* High crystallinity design of Ir-based catalysts drives catalytic reversibility for water electrolysis and fuel cells. *Nat. Commun.* **12**, 1-10 (2021).
10. Lee, E. & Fokwa, B. P. Nonprecious metal borides: emerging electrocatalysts for hydrogen production. *Acc. Chem. Res.*, 5575-5578 (2021).
11. Zhang, J. *et al.* Interface-promoted dehydrogenation and water-gas shift toward high-efficient H_2 production from aqueous phase reforming of cellulose. *ACS Sustainable Chemistry & Engineering*. **6**, 7313-7324 (2018).
12. Li, S. *et al.* Strategies to improve electrocatalytic and photocatalytic performance of two-dimensional materials for hydrogen evolution reaction. *Chinese Journal of Catalysis*. **42**, 511-556 (2021).
13. Yan, B. *et al.* Ru species supported on MOF-derived N-doped TiO_2/C hybrids as efficient electrocatalytic/photocatalytic hydrogen evolution reaction catalysts. *Adv. Funct. Mater.* **30**, 2003007 (2020).
14. You, B. *et al.* Electrocatalytic and photocatalytic hydrogen evolution integrated with organic oxidation. *Chem. Commun.* **54**, 5943-5955 (2018).
15. Khare, R. *et al.* Development of photochemical and electrochemical cells for operando X-ray absorption spectroscopy during photocatalytic and electrocatalytic reactions. *Phys. Chem. Chem. Phys.* **22**, 18891-18901 (2020).
16. Trincado, M. *et al.* Homogeneously catalysed conversion of aqueous formaldehyde to H_2 and carbonate. *Nat. Commun.* **8**, 1-11 (2017).
17. Belhadj, H. *et al.* Mechanisms of simultaneous hydrogen production and formaldehyde oxidation in H_2O and D_2O over platinized TiO_2. *Acs Catalysis*. **7**, 4753-4758 (2017).
18. Wang, K. *et al.* Single-atom VN charge-transfer bridge on ultrathin carbon nitride for efficient photocatalytic H_2 production and formaldehyde oxidation under visible light. *Chem. Eng. J.* **429**, 132229 (2022).
19. Miao, L. *et al.* Ultrathin MnO_2 nanosheets for optimized hydrogen evolution via formaldehyde reforming in water at room temperature. *Applied Catalysis B: Environmental*. **248**, 466-476 (2019).
20. Gao, H. *et al.* Highly efficient hydrogen production and formaldehyde degradation by Cu_2O microcrystals. *Applied Catalysis B: Environmental*. **172**,

1-6 (2015).
21. Heim, L. E. *et al.* Selective and mild hydrogen production using water and formaldehyde. *Nat. Commun.* **5**, 1-8 (2014).
22. Gao, S. T. *et al.* Immobilizing AgPd alloy on Vulcan XC-72 carbon: a novel catalyst for highly efficient hydrogen generation from formaldehyde aqueous solution. *Rsc Advances*. **6**, 105638-105643 (2016).
23. Patra, S. *et al.* Hydrogen Production from Formaldehyde and Paraformaldehyde in Water under Additive-Free Conditions: Catalytic Reactions and Mechanistic Insights. *Inorg. Chem.* **61**, 4618-4626 (2022).
24. Patra, S. & Singh, S. K. Hydrogen Production from Formic Acid and Formaldehyde over Ruthenium Catalysts in Water. *Inorg. Chem.* **59**, 4234-4243 (2020).
25. Zhu, X. H. *et al.* Tandem catalysis induced by hollow PdO: highly efficient H_2 generation coupled with organic dye degradation via sodium formate reforming. *Catalysis Science & Technology*. **8**, 6217-6227 (2018).
26. Peng, S. *et al.* MnO_2-decorated N-doped carbon nanotube with boosted activity for low-temperature oxidation of formaldehyde. *J. Hazard. Mater.* **396**, 122750 (2020).
27. Yao, Y. F. & Wang, G. C. Mechanism insights into the aerobic oxidation of 5-hydroxymethylfurfural to 2, 5-furandicarboxylic acid over MnO_2 catalysts. *The Journal of Physical Chemistry C*. **125**, 3818-3826 (2021).
28. Yang, R. *et al.* MnO_2-based materials for environmental applications. *Adv. Mater.* **33**, 2004862 (2021).
29. Liu, F. *et al.* One-step synthesis of nanocarbon-decorated MnO_2 with superior activity for indoor formaldehyde removal at room temperature. *Applied Catalysis B: Environmental*. **235**, 158-167 (2018).
30. Zou, N. *et al.* Electrothermal regeneration by Joule heat effect on carbon cloth based MnO_2 catalyst for long-term formaldehyde removal. *Chem. Eng. J.* **357**, 1-10 (2019).
31. Zhu, G. *et al.* Encapsulate α-MnO_2 nanofiber within graphene layer to tune surface electronic structure for efficient ozone decomposition. *Nat. Commun.* **12**, 1-10 (2021).
32. Zeng, X. *et al.* Graphene enhanced α-MnO_2 for photothermal catalytic decomposition of carcinogen formaldehyde. *Chin. Chem. Lett.* (2022).
33. Lu, L. *et al.* Graphene–MnO_2 hybrid nanostructure as a new catalyst for formaldehyde oxidation. *The Journal of Physical Chemistry C*. **120**, 23660-23668 (2016).
34. Lu, L. *et al.* Graphene-MnO_2 hybrid nanostructure as a new catalyst for formaldehyde oxidation. *The Journal of Physical Chemistry C*. **120**, 23660-23668 (2016).
35. Chen, B. B. *et al.* Investigation into the catalytic roles of various oxygen species over different crystal phases of MnO_2 for C_6H_6 and HCHO oxidation. *Acs Catalysis*. **10**, 6176-6187 (2020).

36. Liang, S. *et al.* Effect of phase structure of MnO_2 nanorod catalyst on the activity for CO oxidation. *The Journal of Physical Chemistry C*. **112**, 5307-5315 (2008).
37. Fu, X. *et al.* Manganese oxide hollow structures with different phases: Synthesis, characterization and catalytic application. *Catal. Commun.* **10**, 1844-1848 (2009).
38. Cheng, L. *et al.* Boosting acetone oxidation efficiency over MnO2 nanorods by tailoring crystal phases. *New J. Chem.* **43**, 19126-19136 (2019).
39. Yang, W. H. *et al.* Comparative study of alpha-, beta-, gamma- and delta-MnO_2 on toluene oxidation: Oxygen vacancies and reaction intermediates. *Appl Catal B-Environ*. **260** (2020).
40. Zhou, J. *et al.* Oriented growth of layered-MnO_2 nanosheets over α-MnO_2 nanotubes for enhanced room-temperature HCHO oxidation. *Applied Catalysis B: Environmental*. **207**, 233-243 (2017).
41. Okamoto, H. *et al.* Hydrogen evolution from alkaline formaldehyde solution. *Bull. Chem. Soc. Jpn.* **56**, 925-926 (1983).
42. Ashby, E. C. *et al.* Concerning the formation of hydrogen in nuclear waste. Quantitative generation of hydrogen via a Cannizzaro intermediate. *J. Am. Chem. Soc.* **115**, 1171-1173 (1993).
43. Preti, D. *et al.* Aerobic, copper-mediated oxidation of alkaline formaldehyde to fuel-cell grade hydrogen and formate: Mechanism and applications. *Angewandte Chemie-International Edition*. **48**, 4763-4766 (2009).
44. Munusamy, T. D. *et al.* Sustainable hydrogen production by CdO/exfoliated g-C_3N_4 via photoreforming of formaldehyde containing wastewater. *Int. J. Hydrogen Energy*. **46**, 30988-30999 (2021).
45. Chen, X. *et al.* Base-free hydrogen generation from formaldehyde and water catalyzed by copper nanoparticles embedded on carbon sheets. *Catalysis Science & Technology*. **9**, 783-788 (2019).
46. Chen, S. *et al.* Rationally tuning the active sites of copper-based catalysts towards formaldehyde reforming into hydrogen. *Sustainable Energy & Fuels*. **5**, 6470-6477 (2021).
47. Du, L. L. *et al.* Interface engineering of palladium and zinc oxide nanorods with strong metal-support interactions for enhanced hydrogen production from base-free formaldehyde solution. *Journal of Materials Chemistry A*. **7**, 8855-8864 (2019).
48. Qian, K. C. *et al.* Directional oxygen activation by oxygen-vacancy-rich WO_2 nanorods for superb hydrogen evolution via formaldehyde reforming. *Journal of Materials Chemistry A*. **7**, 14592-14601 (2019).
49. Li, R. H. *et al.* Single component gold on protonated titanate nanotubes for surface-charge-mediated, additive-free dehydrogenation of formic acid into hydrogen. *Rsc Advances*. **6**, 100103-100107 (2016).
50. Miao, L. *et al.* Ultrathin MnO_2 nanosheets for optimized hydrogen evolution via formaldehyde reforming in water at room temperature. *Appl Catal B-*

Environ. **248**, 466-476 (2019).
51. Li, R. *et al.* Oxygen-controlled hydrogen evolution reaction: Molecular oxygen promotes hydrogen production from formaldehyde solution using Ag/MgO nanocatalyst. *ACS Catalysis*. **7**, 1478-1484 (2017).
52. Zhang, J. M. *et al.* The interplay of Ag and ferromagnetic $MgFe_2O_4$ for optimized oxygen-promoted hydrogen evolution via formaldehyde reforming. *Catalysis Science & Technology*. **11**, 6462-6469 (2021).
53. Yan, X. Q. *et al.* The interplay of Au nanoparticles and ZnO nanorods for oxygen-promoted, base-free, complete formaldehyde reforming into H_2 and CO_2. *Catal. Commun.* **117**, 5-8 (2018).
54. Chen, S. *et al.* Ultrasmall silver clusters stabilized on MgO for robust oxygen-promoted hydrogen production from formaldehyde reforming. *ACS Appl. Mater. Interfaces*. **11**, 33946-33954 (2019).
55. Liu, H. X. *et al.* High efficient photocatalytic hydrogen evolution from formaldehyde over sensitized Ag@Ag-Pd alloy catalyst under visible light irradiation. *Appl Catal B-Environ*. **237**, 563-573 (2018).
56. Huang, X. *et al.* Au-Pd separation enhances bimetallic catalysis of alcohol oxidation. *Nature*. **603**, 271–275 (2022).
57. Dawson, J. A. *et al.* First-Principles Calculations of Oxygen Vacancy Formation and Metallic Behavior at a β-MnO_2 Grain Boundary. *ACS Appl. Mater. Interfaces*. **7** (2015).
58. Zhang, H. *et al.* DFT calculations of the synergistic effect of λ-MnO_2/graphene composites for electrochemical adsorption of lithium ions. *Phys. Chem. Chem. Phys.* **21**, 8133-8140 (2019).
59. Bucko, T. *et al.* Improved description of the structure of molecular and layered crystals: ab initio DFT calculations with van der Waals corrections. *The Journal of Physical Chemistry A*. **114**, 11814-11824 (2010).
60. Kresse, G. & Furthmüller, J. Efficiency of ab-initio total energy calculations for metals and semiconductors using a plane-wave basis set. *Computational materials science*. **6**, 15-50 (1996).
61. Hammer, B. *et al.* Improved adsorption energetics within density-functional theory using revised Perdew-Burke-Ernzerhof functionals. *Physical Review B*. **59**, 7413-7421 (1999).
62. Blochl, P. E. *et al.* Improved tetrahedron method for Brillouin-zone integrations. *Physical Review B*. **49**, 16223-16233 (1994).
63. Perdew, J. P. *et al.* Generalized gradient approximation made simple. *Phys. Rev. Lett.* **77**, 3865 (1996).
64. Grimme, S. *et al.* Effect of the damping function in dispersion corrected density functional theory. *J. Comput. Chem.* **32**, 1456-1465 (2011).
65. Li, G. F. *et al.* Research on the removal mechanism of antimony on alpha-MnO_2 nanorod in aqueous solution: DFT plus U method. *J. Hazard. Mater.* **354**, 8-16 (2018).
66. Ong, S. P. *et al.* Voltage, stability and diffusion barrier differences between

sodium-ion and lithium-ion intercalation materials. *Energy & Environmental Science*. **4**, 3680-3688 (2011).

Acknowledgments

P.P.Z., H.L.S., X.Z., and T.Z. would like to thank Xiamen University, College of Chemistry and Chemical Engineering for financial support. Xiuyuan Lu (CSC No. 201806370221) is financially supported by a Ph.D. scholarship from China Scholarship Council. A.R. thanks the UK's HPC Materials Chemistry Consortium (EP/L000202, EP/R029431), UK Molecular Modelling Hub (EP/T022213/1), and the Advanced Research Computing @ Cardiff (ARCCA). X.Y.H. acknowledges the support from （NRF) Brain Pool Program.

Author Contributions

P.P.Z. and X.Y.H. conceived the design of the project. P.P.Z. prepared catalytic materials and performed thermal and electrochemical experiments. P.P.Z., H.L.S., and X.Z. performed the characterisations of materials, including TEM-elemental mapping, SEM, XRD, XPS, BET surface area measurement, *et al*. X.Y.L., A.R. developed the DFT model and calculations. X.Y.H., B.H.C. directed the research. X.Y.H., P.P.Z., and X.Y.L. wrote the manuscript and the corresponding supporting information. All authors have contributed to the manuscript and the data analysis.

Ethics declarations

The authors declare no competing interests.